

This discussion paper is/has been under review for the journal Atmospheric Chemistry and Physics (ACP). Please refer to the corresponding final paper in ACP if available.

Spatio-temporal variability of water vapor investigated by lidar and FTIR vertical soundings above Mt. Zugspitze

H. Vogelmann, R. Süssmann, T. Trickl, and A. Reichert

Karlsruhe Institute of Technology, IMK-IFU, Garmisch-Partenkirchen, Germany

Received: 18 August 2014 – Accepted: 16 October 2014 – Published: 14 November 2014

Correspondence to: H. Vogelmann (hannes.vogelmann@kit.edu)

Published by Copernicus Publications on behalf of the European Geosciences Union.

ACPD
14, 28231–28268, 2014

Spatio-temporal variability of water vapor

H. Vogelmann et al.

Title Page	Introduction
Abstract	References
Conclusions	Tables
Tables	Figures
 	 
 	 
Back	Close
Full Screen / Esc	
Printer-friendly Version	
Interactive Discussion	



Abstract

Water vapor is the most important greenhouse gas and its spatio-temporal variability strongly exceeds that of all other greenhouse gases. However, this variability has hardly been studied quantitatively so far. We present an analysis of a five-year period of water vapor measurements in the free troposphere above Mt. Zugspitze (2962 m a.s.l., Germany). Our results are obtained from a combination of measurements of vertically integrated water vapor (IWV), recorded with a solar Fourier Transform InfraRed (FTIR) spectrometer on the summit of Mt. Zugspitze and of water vapor profiles recorded with the nearby differential absorption lidar (DIAL) at the Schneefernerhaus research station. The special geometrical arrangement of one zenith-viewing and one sun-pointing instrument and the temporal resolution of both instruments allow for an investigation of the spatio-temporal variability of IWV on a spatial scale of less than one kilometer and on a time scale of less than one hour. The SD of differences between both instruments σ_{IWV} calculated for varied subsets of data serves as a measure of variability. The different subsets are based on various spatial and temporal matching criteria. Within a time interval of 20 min, the spatial variability becomes significant for horizontal distances above 2 km, but only in the warm season ($\sigma_{\text{IWV}} = 0.35 \text{ mm}$). However, it is not sensitive to the horizontal distance during the winter season. The variability of IWV within a time interval of 30 min peaks in July and August ($\sigma_{\text{IWV}} > 0.55 \text{ mm}$, mean horizontal distance = 2.5 km) and has its minimum around midwinter ($\sigma_{\text{IWV}} < 0.2 \text{ mm}$, mean distance > 5 km). The temporal variability of IWV is derived by selecting subsets of data from both instruments with optimal volume matching. For a short time interval of 5 min, the variability is 0.05 mm and increases to more than 0.5 mm for a time interval of 15 h. The profile variability of water vapor is determined by analyzing subsets of water vapor profiles recorded by the DIAL within time intervals from 1 to 5 h. For all altitudes, the variability increases with widened time intervals. The lowest relative variability is observed in the lower free troposphere around an altitude of 4.5 km. Above 5 km, the relative variability increases continuously up to the tropopause by about a factor of 3.

Spatio-temporal variability of water vapor

H. Vogelmann et al.

[Title Page](#)

[Abstract](#)

[Introduction](#)

[Conclusions](#)

[References](#)

[Tables](#)

[Figures](#)

◀

▶

◀

▶

[Back](#)

[Close](#)

[Full Screen / Esc](#)

[Printer-friendly Version](#)

[Interactive Discussion](#)



Spatio-temporal variability of water vapor

H. Vogelmann et al.

[Title Page](#)[Abstract](#)[Introduction](#)[Conclusions](#)[References](#)[Tables](#)[Figures](#)[◀](#)[▶](#)[◀](#)[▶](#)[Back](#)[Close](#)[Full Screen / Esc](#)[Printer-friendly Version](#)[Interactive Discussion](#)

Analysis of the covariance of the vertical variability reveals an enhanced variability of water vapor in the upper troposphere above 6 km. It is attributed to a more coherent flow of heterogeneous air masses, while the variability at lower altitudes is also driven by local atmospheric dynamics. By studying the short-term variability of vertical water

5 vapor profiles recorded within a day, we come to the conclusion that the contribution of long-range transport and the advection of heterogeneous layer structures may exceed the impact of local convection by one order of magnitude even in the altitude range between 3 and 5 km.

1 Introduction

10 Water vapor plays a key role in weather and climate phenomena and is the most important greenhouse gas (e.g., Harries, 1997; Kiehl and Trenberth, 1997; Trenberth et al., 2007). However, the feedback between the anthropogenic (CO_2 -driven) temperature increase and the influence of water vapor is far from being understood (eg. Wagner et al., 2006). Furthermore, climate projections still suffer from inaccurate parameterizations of water vapor absorption processes within the radiation code of general circulation models (e.g. Turner and Mlawer, 2010). Understanding the role of water vapor in the climate system is particularly complex because water vapor is the only trace compound in the atmosphere showing up in all three states of matter. This has a variety of implications, e.g. the possibility of transporting latent heat (thereby damping latitudinal temperature gradients) or the fact that precipitation is the largest sink of atmospheric water vapor. The latter is the main reason of the strong decrease of water vapor concentration with altitude, and it is the reason why water vapor has an average life time in the atmosphere of just about 9 days which is shorter than for any other greenhouse gas. The short life-time is a basis of the very high spatio-temporal variability of water vapor (Trenberth, 1998).

25 However, the spatio-temporal variability of water vapor on the scales relevant to weather and climate is still far from being quantitatively characterized, and the un-

derlying processes are not well understood. Variability, for instance, may be caused by local dynamics above complex mountain terrain (which changes with season), by regional meteorological effects, or by the advection on larger scales. A highly interesting question is the variance of water vapor as a function of altitude on different time scales.

- 5 Previous studies at our site based on ozone and aerosol lidar profiling demonstrated that the free troposphere may be affected by regional contributions, long-range transport, and stratosphere–troposphere exchange causing strongly and rapidly changing vertical structures in the concentration profile (Eisele et al., 1999; Stohl and Trickl, 1999; Trickl et al., 2003; Trickl et al., 2010, 2011). In particular, we frequently observe
10 very dry and sometimes very thin layers in the free troposphere, which were associated with stratospheric intrusion events. It remains open, however, how much such processes significantly contribute to the observed variability of water vapor in the middle and upper troposphere.

For understanding the long-term changes and the variability of water vapor, high-quality vertical sounding of water vapor with high temporal density is required. During the past years, a variety of optical remote sounders has been developed for this purpose in addition to the classical radiosondes (e.g. Kämpfer, 2013). Lidars, Fourier-transform-infrared (FTIR) spectrometers, and microwave radiometers fulfill the requirements of frequent measurements. In particular, we developed a differential absorption lidar (DIAL) for use at Mt. Zugspitze, which allows for continuous day- and nighttime soundings of water vapor profiles up to the tropopause (Vogelmann and Trickl, 2008). For measuring integrated water vapor (I WV), the solar FTIR technique was found to be one of the most accurate and precise ground-based sounding techniques with a precision better than 0.05 mm (2.2 % of the mean) (Sussmann et al., 2009). According to
20 25 a recent validation study, the lidar and FTIR water vapor sounders used for the work presented here are in excellent agreement (Vogelmann et al., 2011).

Comparing two high-precision state-of the art water vapor sounders, we also found that it is necessary to use very strict temporal coincidence criteria on the time scale of minutes and a spatial matching on the scale of 100 m. Otherwise, the combined

Spatio-temporal variability of water vapor

H. Vogelmann et al.

[Title Page](#)

[Abstract](#)

[Introduction](#)

[Conclusions](#)

[References](#)

[Tables](#)

[Figures](#)

◀

▶

◀

▶

[Back](#)

[Close](#)

[Full Screen / Esc](#)

[Printer-friendly Version](#)

[Interactive Discussion](#)



precision of the instruments will be affected by the natural variability of water vapor (Sussmann et al., 2009; Vogelmann et al., 2011). This was confirmed by Bleisch et al. (2011) who reported that in case of long distances between the locations of the intercompared instruments, atmospheric variability tends to blur out the significance of validation results. The question of co-location has also become an issue in the Global Climate Observing System (GCOS) Reference Upper Air Network (GRUAN) (Immler et al., 2010; Sun et al., 2010; Seidel et al., 2011; Fassò et al., 2014) and it was addressed when evaluating water vapor sounding validation campaigns like MOHAVE (2009), LUAMI (2008), WAVES (2006), AWEX-G (2003) (Leblanc et al., 2011; Stiller et al., 2012; Wirth et al., 2009; Adam et al., 2010; Whiteman et al., 2006). Co-location also is of relevance to ground-based validation of satellite missions and has been addressed many times (e.g. Tobin et al., 2006; Soden and Lanzante, 1996).

The goal of this paper is to derive quantitative information relating to the spatio-temporal variability of water vapor. The solar FTIR spectrometer on the summit of Mt. Zugspitze (2962 m a.s.l.) and the DIAL located only 680 m to the southwest and about 288 m below provide a unique geometrical arrangement of two high-precision water vapor sounders, allowing for an advanced analysis of the spatio-temporal variability of integrated water vapor (IWV) on small scales ($\Delta t < 1$ h, $\Delta x < 1$ km).

After a brief description of the instrumental setup as well as of the FTIR and DIAL IWV data with their geometrical and temporal properties, we present the quantification of the spatial and temporal variability of IWV by a statistical analysis of selected subsets of IWV data from the FTIR and the DIAL (Sects. 3.1 and 3.2). The profile-type variability of the vertical water vapor distribution is analyzed quantitatively by examining selected subsets of DIAL soundings and by calculating a profile covariance matrix (Sect. 4). Different mechanisms driving the short-term variability of water vapor are investigated in four case studies (Sect. 5). Finally, major results are summarized (Sect. 6).

Spatio-temporal
variability of water
vapor

H. Vogelmann et al.

[Title Page](#)

[Abstract](#)

[Introduction](#)

[Conclusions](#)

[References](#)

[Tables](#)

[Figures](#)

◀

▶

◀

▶

[Back](#)

[Close](#)

[Full Screen / Esc](#)

[Printer-friendly Version](#)

[Interactive Discussion](#)



2 Instrumentation and geographical arrangement

2.1 Zugspitze solar FTIR system

Solar absorption FTIR spectrometry uses the direct radiation from the sun in the mid-infrared range as a light source. The FTIR provides total columns of numerous atmospheric trace gases. Additionally, information on the vertical distribution of trace gases can be derived (typically 2–3 degrees of freedom in a retrieval optimized for IWV) from the shape of the pressure-broadened infrared lines. Due to its principle, the solar FTIR measures slant columns/profiles pointing towards the actual position of the sun. The FTIR instrument (Table 1) located on the summit of Mt. Zugspitze is based on a Bruker IFS125HR interferometer and is described in detail by Sussmann and Schäfer (1997). The retrieval of IWV is based on the SFIT 2 algorithm (Pougatchev et al., 1995), which is the standard code of the Network for the Detection of Atmospheric Composition Change (NDACC). An FTIR retrieval optimized for IWV was developed recently by Sussmann et al. (2009). The precision of the IWV retrieval was estimated to be better than 0.05 mm (2.2 % of the mean).

2.2 Differential absorption lidar (DIAL)

DIAL is a laser-based remote sensing technique providing number-density profiles of trace gases. Measurements are based on the specific molecular absorption and the well-established spectroscopy. The Zugspitze DIAL is operated with single absorption lines in the 817 nm band of H₂O (Table 1) for ground-based water vapor profiling in the free troposphere. In order to keep a balanced signal-to-noise ratio a vertical resolution (VDI Guideline 4210) of 50 to 300 m is adapted dynamically to the vertical range from 2.95 km to roughly 12 km a.s.l., respectively. The DIAL instrument is located at the Schneefernerhaus research station (UFS) on the steep southern slope of Mt. Zugspitze at an altitude of 2675 m a.s.l. The range of the Zugspitze DIAL starts 250 m above the laboratory, slightly below the altitude of the FTIR spectrometer. The DIAL system at

Title Page	
Abstract	Introduction
Conclusions	References
Tables	Figures
◀	▶
◀	▶
Back	Close
Full Screen / Esc	
Printer-friendly Version	
Interactive Discussion	



[Title Page](#)[Abstract](#)[Introduction](#)[Conclusions](#)[References](#)[Tables](#)[Figures](#)[◀](#)[▶](#)[◀](#)[▶](#)[Back](#)[Close](#)[Full Screen / Esc](#)[Printer-friendly Version](#)[Interactive Discussion](#)

Schneefernerhaus/Zugspitze and the retrieval of water vapor profiles are described in more detail by Vogelmann and Trickl (2008). Water vapor profiles from the Zugspitze DIAL are also a very good basis for the calculation of IWV with a precision better than 0.1 mm (Vogelmann et al., 2011).

5 2.3 Geographical setup and IWV data selection

The Zugspitze (47.42° N, 10.98° E, 2962 m a.s.l.) is by far the highest mountain on the northern rim of the Alps. The free troposphere above this site is representative of Central Europe. The mountain is above the moist boundary layer for most of the year. Due to reduced absorption losses this site is ideal for sensitive spectroscopic measurements 10 of water vapor throughout the free troposphere. While the FTIR instrument is located on the summit of Mt. Zugspitze the DIAL instrument is located at the Schneefernerhaus research station (UFS) on the steep southern slope of Mt. Zugspitze at an altitude of 2675 m a.s.l., 680 m southwest of the FTIR instrument (Fig. 1).

The sun-pointing geometry of the FTIR instrument and the fixed zenith-pointing geometry of the DIAL allows for studies of the differences of IWV values measured by both instruments with a defined spatial and temporal matching (Fig. 1). According to reanalysis data from the National Center for Environmental Prediction (NCEP), the center of gravity of the water vapor vertical distribution above Mt. Zugspitze most frequently is located at a rather constant altitude between 4300 m a.s.l. in summer and 4400 m a.s.l. 15 in winter. For simplicity, it is assumed that the FTIR IWV is horizontally located at the point where the viewing direction of the instrument meets the altitude level of the center of gravity of the IWV distribution. This assumption, of course, describes the reality at high sun elevation angles better. From this and the actual position of the sun, a rough estimate of the varying horizontal position of the IWV measured by the FTIR instrument 20 is possible. The zenith angle of the sun defines the horizontal distance from the instrument, which may vary from less than 1 km around noon in midsummer to more than 10 km at very low sun positions. The azimuth of the FTIR IWV position is equal to the azimuth of the sun position which depends on daytime and season. In contrast to this,

Spatio-temporal variability of water vapor

H. Vogelmann et al.

Title Page	
Abstract	Introduction
Conclusions	References
Tables	Figures
◀	▶
◀	▶
Back	Close
Full Screen / Esc	
Printer-friendly Version	
Interactive Discussion	



the horizontal position of IWV measured with the DIAL is always fixed to the location of the instrument, 680 m southwest of the FTIR site. This is illustrated in Fig. 1.

Figure 2 shows the horizontal allocation of all FTIR IWV measurements recorded in coincidence ($\Delta t \leq 30$ min) with a DIAL measurement. The horizontal distance between the location of the DIAL and the horizontal position of the IWV measured by the FTIR is defined as spatial matching Δx . Figure 2 also shows the daily trajectories of the horizontal position of the center of gravity of IWV probed with the FTIR instrument for midsummer, equinox, and midwinter. In the summer season, the mean horizontal distance Δx is obviously smaller than during winter (see also dashed curve in Fig. 4).

10 3 Variability of integrated water vapor in space and time

Of more than 350 lidar profiles recorded in the years 2007–2009, more than 250 profiles were measured during daytime (i.e. between 05:00 and 19:00 LT). In the same period, more than 3500 column measurements were made by the FTIR instrument. The systems operate with a typical integration time of 13 min (FTIR) and 17 min (DIAL).
15 In order to obtain a quantitative measure of the water vapor variability we calculate the SD of the differences σ_{IWV} between the IWV values recorded by the two different instruments under certain spatio-temporal matching criteria Δx and Δt .

3.1 Spatial variability

We decided to analyze the spatial and temporal variabilities separately for summer and winter because of two counteracting effects:
20

1. The special observation geometry in this study implies that the spatial overlap Δx of both soundings depends on both daytime and season. As shown in Figs. 1, 2 and 4 (dashed curve), the best spatial matching ($\Delta x < 1$ km) is achieved around midsummer in the early afternoon only (between 12:00 and 14:00 UTC), while Δx is always larger during the winter season.
25

2. Due to heat-driven convective dynamics in complex mountain surroundings, spatial and temporal variabilities of IWV are expected to be higher during summer and lower during winter.

For determining the spatial variability of IWV, we calculated σ_{IWV} as a function of varied spatial matching Δx by using measurement pairs within a time interval of $\Delta t = 30\text{ min}$ (summer) and $\Delta t = 60\text{ min}$ (winter). As mentioned above, it was shown that for a good agreement of both systems very tight spatial and temporal matching criteria are mandatory (Vogelmann et al., 2011). Figure 3 (red curve) shows σ_{IWV} as a function of the horizontal distance of the probed volumes in the summer season. While σ_{IWV} constantly remains around 0.35 mm for $\Delta x < 2\text{ km}$, it rises to values of more than 0.65 mm at a distance of $\Delta x = 4\text{ km}$. This result shows that the variability depends on the spatio-temporal matching. Up to $\Delta x = 2\text{ km}$, the temporal variability within the selected time interval ($\Delta t = 30\text{ min}$) predominates. For larger distances, the contribution of spatial variability becomes significant.

In contrast to this, σ_{IWV} is not increasing with Δx in the winter season (Fig. 3, blue curve). This is in agreement with the assumption that local convection does not reach the vertical measurement range during the winter season and that the IWV variability is probably dominated by horizontal advection of filamentary structures in the free troposphere from very different source regions. Consequently, the observed variability during winter is due to larger spatial scale processes (compared to local convection in summer), which would explain the absence of an increase with Δx in Fig. 3. Note that because IWV is much lower in winter than in summer, the relative variabilities (i.e. if σ_{IWV} were given in per cent) would be larger for the blue curve in Fig. 3. This means that advection of filaments (winter) leads to larger relative changes of IWV than local convection in summer. We will discuss this finding in more detail within the context of the variability of the vertical water vapor profile in Sect. 4. Figure 3 also indicates that σ_{IWV} even shows a trend to lower values for distances above 6 km. We explain this by the fact that measurements with large horizontal mismatch ($\Delta x > 6\text{ km}$) require ex-

Spatio-temporal variability of water vapor

H. Vogelmann et al.

[Title Page](#)

[Abstract](#)

[Introduction](#)

[Conclusions](#)

[References](#)

[Tables](#)

[Figures](#)

◀

▶

◀

▶

[Back](#)

[Close](#)

[Full Screen / Esc](#)

[Printer-friendly Version](#)

[Interactive Discussion](#)



Spatio-temporal variability of water vapor

H. Vogelmann et al.

[Title Page](#)

[Abstract](#)

[Introduction](#)

[Conclusions](#)

[References](#)

[Tables](#)

[Figures](#)

◀

▶

◀

▶

[Back](#)

[Close](#)

[Full Screen / Esc](#)

[Printer-friendly Version](#)

[Interactive Discussion](#)



extraordinarily calm and clear weather conditions, because the FTIR instrument requires a cloudless field of view and a sun position close to the horizon.

Figure 4 shows σ_{IWV} as a function of the Julian day. Here, counteracting effects can be observed. While the mean horizontal distance (dashed curve) is low in the summer season ($\Delta x < 2 \text{ km}$), it reaches up to almost 10 km around midwinter. The variability over the entire field of horizontal distances within a certain time interval (e.g. 20 min) reaches its maximum of almost 0.6 mm when the temperature peaks around the end of July. We assume that this is a direct effect of the heat-driven local convection, which can reach altitudes of 4.5 km at our site during the summer season (Reiter et al., 1983; Müller and Reiter, 1986; Carnuth and Trickl, 2000; Carnuth et al., 2002; Kreipl, 2006). The fact that the maximum variability is found close to the minimum average distance indicates that the former is caused by local effects. The minimum variability of about 0.15 mm is observed around midwinter when temperatures are low, although the mean horizontal mismatch of both instruments is largest at this time of the year.

3.2 Temporal variability

For the analysis of temporal variability, we calculated the SD of differences σ_{IWV} between IWV values from both instruments as a function of temporal coincidence. This was repeated for varied spatial matching criteria. When using all IWV values from both instruments without applying any geometrical matching criteria, σ_{IWV} shows a flat minimum around a coincidence interval of $\Delta t = 20 \text{ min}$, see red curve in Fig. 5. About 100–300 coincident pairs contribute to the ensembles within this minimum. At first, a minimal σ_{IWV} for the shortest interval length would be expected. Two different effects are responsible for the minimum around $\Delta t = 20 \text{ min}$. First of all, most FTIR and lidar measurements were carried out in the morning, because there are still few clouds. As a consequence, most of the pairs with the shortest coincidence intervals are found in the morning where the spatial matching is worst (see Figs. 1 and 2). This slightly increases σ_{IWV} on the very left hand side of the red curve in Fig. 5. Secondly, many pairs with good spatial matching can be found around noon, even for somewhat larger tem-

Spatio-temporal variability of water vapor

H. Vogelmann et al.

[Title Page](#)[Abstract](#)[Introduction](#)[Conclusions](#)[References](#)[Tables](#)[Figures](#)[|◀](#)[▶|](#)[◀](#)[▶](#)[Back](#)[Close](#)[Full Screen / Esc](#)[Printer-friendly Version](#)[Interactive Discussion](#)

poral coincidence intervals. This explains the decrease of σ_{IWV} towards the minimum (red curve in Fig. 5).

When considering measurement pairs with an FTIR sun azimuth close to the position of the DIAL instrument ($210 \pm 6^\circ$) only, σ_{IWV} is much smaller in general and has its minimum at the shortest coincidence intervals (green curve in Fig. 5). For time intervals on the minutes scale, we find $\sigma_{\text{IWV}} = 0.05 \text{ mm}$, which agrees with the validated (combined) precision of our instruments Vogelmann et al. (2011).

The temporal variability of IWV can also be estimated from the SD of differences of measurements recorded by the same instrument within certain time intervals. In our case, this was possible with data from the FTIR instrument only, thanks to its more frequent and continuous operation. The result is reflected by the blue curve in Fig. 5. Due to the solar FTIR's 13.3 min integration time, the curve starts at an interval length of $\Delta t = 20 \text{ min}$. The blue curve begins to deviate increasingly from the green curve beyond 30 min and converges towards the red curve for larger time intervals. This corresponds to the fact that we observe a superposition of temporal and spatial variability with the solar FTIR, i.e., for larger time intervals, the FTIR instrument produces a spatial mismatch by itself: due to its sun-pointing geometry, the FTIR instrument probes a different volume after a certain time. This spatial mismatch has a significant effect for time intervals longer than 30 min.

20 4 Profile variability

The variability of the vertical water vapor distribution on time scales of $\Delta t \leq 5 \text{ h}$ was derived from water vapor number density profiles retrieved from the DIAL measurements. We built ensembles of DIAL water vapor profiles recorded within a range of time intervals (e.g. 1–5 h). After normalizing each profile by the respective ensemble mean profile, we merged all normalized profiles into a large ensemble for statistical analysis. First, we calculated the relative variance σ^2/μ^2 (with $\mu = \text{ensemble mean number density}$) as a function of altitude for different time intervals. This is plotted on the left

hand side of Fig. 6. For the shortest time interval of this investigation (1 h), the relative variance starts with a value of about 0.02. Above 5 km, the variance continuously increases to more than 0.38 at an altitude of about 11 km a.s.l. For longer time intervals up to 5 h, the relative variance behaves quite similarly, but is shifted to higher values at all altitudes. This is in agreement with our results of IWV variability analysis, according to which longer time intervals lead to larger variabilities. In comparison to the 1 h profile, we see a more significant maximum at the lower edge at 3 km and a significant minimum at 4.5 km for longer time intervals. This enhanced increase between 3 and 4 km is, to our understanding, induced by the diurnally varying upper edge of the boundary layer during the warm season (see below).

For the lowest layer (i.e. 3–4 km), where most of the entire column above our site is stored, we find equal relative variabilities as for IWV. This means that for a time interval $\Delta t = 1$ h, the coefficient of variation $\sigma/\mu = 0.12$. From the green curve in Fig. 5, we obtain a 1 h variability of 0.27 mm with a 60 min ensemble mean IWV of 2.33 mm, which also yields a coefficient of variation of 0.12.

In contrast to this, the relative variability increases with altitude above 5 km. This can be explained by the increasing wind speed at higher altitudes in the troposphere. The temporal variability of the water vapor density in the free troposphere at a certain altitude primarily features a horizontal variability combined with a horizontal wind velocity at this altitude. From NCEP reanalysis data, we derived an average wind speed as a function of altitude, which increases from a few meters per second near the ground to about 22 m s^{-1} in the tropopause region (Fig. 7). Similar values were reported by Birner et al. (2002) based on radiosonde data recorded above Munich (South Germany). Depending on the pathway of the jet stream or the polar vortex, maximum wind velocities of more than 100 m s^{-1} occur occasionally (Riehl, 1962). Considering a time interval of 60 min, this means a mean horizontal spread of about 80 km around 10 km altitude with a potential increase to more than 360 km in the jet stream regime.

The general increase of the relative short-term variability of water vapor above 5 km (Fig. 6, left) seems to flatten slightly at about 10 km. This can be explained by the fact

Spatio-temporal variability of water vapor

H. Vogelmann et al.

[Title Page](#)

[Abstract](#)

[Introduction](#)

[Conclusions](#)

[References](#)

[Tables](#)

[Figures](#)

◀

▶

◀

▶

[Back](#)

[Close](#)

[Full Screen / Esc](#)

[Printer-friendly Version](#)

[Interactive Discussion](#)



Spatio-temporal variability of water vapor

H. Vogelmann et al.

[Title Page](#)

[Abstract](#)

[Introduction](#)

[Conclusions](#)

[References](#)

[Tables](#)

[Figures](#)

◀

▶

◀

▶

[Back](#)

[Close](#)

[Full Screen / Esc](#)

[Printer-friendly Version](#)

[Interactive Discussion](#)



that the wind speed has its maximum here and decreases at higher altitudes. Above 9 km, the contribution of measurement errors becomes significant. The DIAL is not able to measure water vapor concentrations below 18 ppm (sensitivity limit at 10 km), which may be even lower in the tropopause region. Hence, for the calculation of variances and covariances, only profiles valid in the entire range (3–12 km) are taken into account including a statistical error calculation.

The connectivity of the short-term variability of water vapor at different altitudes is analyzed using the covariance matrix of the vertical profile variability (Fig. 6, right). The covariance matrix is calculated from all normalized profiles recorded from 2007 to 2011, which are contained in the subensembles of profiles recorded within a 5 h time interval. Consequently, the diagonal of the covariance matrix is identical to the 5 h-curve of the variability profile shown on the left hand side of Fig. 6. There are no significant off-diagonal values below 6 km. We interpret this as a sign of the lower altitudes being not dominated by a coherent air flow for most of the observations. This means that the horizontal flow at certain altitudes below 6 km is not or only weakly coupled to the flow above or below. The slight increase of off-diagonal values between 6 and 8 km indicates a partially coherent flow. The high off-diagonal values above 8 km indicate a large fraction of coherent flow of inhomogeneous air masses in this altitude region.

The weak coupling between different layers at lower altitudes is in agreement with the assumption of local convection and turbulence being the dominant sources of variability in the lower part of the examined altitude range. This behavior can be described by barely interacting “bubbles” of humid air. In the upper troposphere, by contrast, varying air masses are more coherently exchanged within the upper air flow, as a result of which layers of a wider vertical spread are affected.

5 Mechanisms driving the variability observed

Evaporation is the only relevant source and precipitation the only relevant sink of water vapor in the troposphere. Thus, water vapor is injected into the free troposphere by up-

lifting processes, such as local convection or large-scale warm conveyor belts. These uplifting processes cause inhomogeneity in the horizontal water vapor distribution at a certain altitude. Furthermore, air ascending to high altitudes undergoes cooling. If this air initially was humid, part of its water vapor content can be precipitated during the ascent. As a result, the absolute humidity of upper tropospheric air is low in general. Downwelling of dry air from high altitudes, in particular from the tropopause region or even the stratosphere, also produces inhomogeneity in the horizontal humidity field at the affected altitude levels. In contrast to uplifting processes, downwelling generally is not a local phenomenon. As regards the short-term variability (i.e. $\Delta t < 6\text{ h}$) of the vertical distribution of water vapor, it is reasonable to distinguish between inhomogeneity produced locally on a small scale and inhomogeneity produced remotely and transported on long-range pathways. By analyzing the measured water vapor profiles in combination with HYSPLIT backward trajectories calculated from reanalysis data (<http://ready.arl.noaa.gov/HYSPLIT.php>, Draxler and Hess, 1998), we found that the short-term variability of the profiles shows contributions from both local effects and long-range transport at the same time. The short-term variability above 5 km can be attributed to the advection of a heterogeneous layer structure in most cases. Below 5 km, by contrast, a clear assignment is not always possible. However, the performance of a trajectory model is also limited above complex terrain. In the following subsections we highlight four different types of dynamics producing short-term variability of water vapor.

5.1 Local convection

5.1.1 Case studies

A case of local convection under stable atmospheric conditions (high pressure) is shown in Fig. 8. Three water vapor profiles were recorded within 40 min. The variability stops at the upper edge of the boundary layer at 3.5 km. Above this level, the water vapor distribution remains constant throughout that period. The upper edge of the

Spatio-temporal variability of water vapor

H. Vogelmann et al.

[Title Page](#)

[Abstract](#)

[Introduction](#)

[Conclusions](#)

[References](#)

[Tables](#)

[Figures](#)

◀

▶

◀

▶

[Back](#)

[Close](#)

[Full Screen / Esc](#)

[Printer-friendly Version](#)

[Interactive Discussion](#)



**Spatio-temporal
variability of water
vapor**

H. Vogelmann et al.

[Title Page](#)[Abstract](#)[Introduction](#)[Conclusions](#)[References](#)[Tables](#)[Figures](#)[◀](#)[▶](#)[◀](#)[▶](#)[Back](#)[Close](#)[Full Screen / Esc](#)[Printer-friendly Version](#)[Interactive Discussion](#)

boundary layer was visually verified by the upper edge of cumulus clouds located at the top of some thermals. Strongly enhanced backscatter from boundary layer aerosols is recorded up to 3.5 km. Some weaker aerosol structure that slowly moves downwards is observed above 4.5 km and even up to 7.1 km.

The situation is somewhat different under conditions of low pressure and atmospheric instability. This case is shown in Fig. 9. Five profiles were recorded within a time interval of 4 h before a heavy thunderstorm developed in the afternoon. The short-term variability of water vapor is rather high and reaches far into the upper troposphere up to at least 7.5 km. Due to the travel time of upwelling air and the increasing horizontal wind speed, the variations at high altitudes (e.g. above 5 km) are less local than the variations near the ground. Cloud formation is first observed between 5.5 and 6.5 km. But only a few minutes later, clouds form also above 2.5 km. Due to cloud interference, the last valid profile was recorded at 11:10 UTC (LT – 1 h). Strongly enhanced backscatter from boundary-layer aerosols was recorded up to 4.7 km in the morning already (07:03 UTC). This altitude is rather high. The latest profile at 11:10 UTC exhibits boundary-layer aerosols up to 4.2 km only and also a lower humidity compared to the profiles recorded before. To our understanding, this indicates a downflow near, but outside of the thunderstorm. This downwelling air probably lost most of its original water content during its ascent in the thunderstorm by precipitation. At 12:37 UTC (profile not shown), the extended head of the cumulonimbus cloud of the upcoming thunderstorm overcasts the site above 7.7 km already. In addition, strong aerosol structures appear up to 7.5 km. Backward trajectory calculations (HYSPLIT) suggest that air between 6 and 7.5 km originated from the Caribbean boundary layer.

5.1.2 General discussion

During the warm season, local convection and “Alpine pumping” usually reach altitudes of up to 1.5 km above summit levels (Carnuth and Trickl, 2000; Carnuth et al., 2002; Kreipl, 2006), which is about 4.5 km a.s.l. in our case. The slightly elevated short-term variability at lower altitudes around 3.5 km (Fig. 6, left) is attributed to local convection

and the diurnal variation of the upper edge of the planetary boundary layer, which is caused by Alpine pumping. Due to the strong vertical gradient of the water vapor profile, this dominates the short-term variability of IWV in most cases when local convection significantly exceeds 3 km (which is the bottom of our measurement range). From the 5 comparatively low mean wind speed at lower altitudes (Fig. 7), we conclude that the elevated variability here is caused by larger horizontal gradients in the water vapor concentration. This means that variations occur on smaller horizontal scales compared to higher altitudes, which underlines that local processes on small scales are the dominant source, e.g. thermal lifts. Short-term variations of the water vapor concentration 10 at a certain altitude within the upper part of the boundary layer (i.e. 3–4.5 km a.s.l.), which are caused by local convection, are estimated to be smaller than a factor of 2. Convection intruding the free troposphere or even the upper troposphere can cause 15 short-term variation factors of more than 5 at these high altitudes (e.g. Fig. 9, other observations). The presence of aerosols (enhanced backscatter) usually indicates up-welling air from the planetary boundary layer. Aerosol structures in the free troposphere are also helpful for estimating the vertical velocity of the probed air.

5.2 Long-range transport

5.2.1 Case studies

Figures 10 and 11 show cases of extreme vertical variability of water vapor on a time 20 scale of hours recorded with the DIAL. Similar scenarios have been observed many times. From these incidents we learned that the water vapor density at a certain altitude can vary by a factor of more than 30 within a few hours. Thus, the short-term variability of water vapor induced by long-range transport and the advection of very in-homogeneous layer structures can exceed the impact of local convection by one order 25 of magnitude.

This is particularly pronounced for stratospheric intrusions that descend from the Arctic to Central Europe. These intrusion layers occasionally become the main source of

Spatio-temporal variability of water vapor

H. Vogelmann et al.

[Title Page](#)

[Abstract](#)

[Introduction](#)

[Conclusions](#)

[References](#)

[Tables](#)

[Figures](#)

◀

▶

◀

▶

[Back](#)

[Close](#)

[Full Screen / Esc](#)

[Printer-friendly Version](#)

[Interactive Discussion](#)



Title Page	
Abstract	Introduction
Conclusions	References
Tables	Figures
◀	▶
◀	▶
Back	Close
Full Screen / Esc	
Printer-friendly Version	
Interactive Discussion	



short-term variability of water vapor in the altitude range between 3 and 5 km. Stratospheric intrusions into the lower free troposphere usually occur in the winter season with a frequency of roughly 4 to 10 times per month above our site (Stohl et al., 2000; Trickl et al., 2010). Under these conditions heterogeneous air masses are usually advected with a high velocity which results in a very high variability at certain altitudes even on the short timescale of one hour. Due to the origin of these layers, stratospheric intrusion events are usually accompanied by rather dry conditions. This is illustrated by the example given in Fig. 10 where three layers of stratospheric air have been advected at the same time at different altitudes, thus, creating relative variations of the water vapor density of more than a factor of 10 at certain altitudes within 4 h. This very complex case is discussed in more detail in a separate publication (Trickl et al., 2014).

Also humid air from remote boundary layers sometimes causes rather intense short-term variations of the water vapor distribution. An example is shown in Fig. 11. Backward trajectory calculations (from reanalysis data) for this case indicate that the origin of the advected air at an altitude of 4.7 km a.s.l. changes from the subarctic upper troposphere (dry) to the Pacific boundary layer (rather humid) within two hours, while the air at an altitude of about 3.3 km constantly originates from the subtropical North Atlantic boundary layer (moderately humid). The trajectory starting in the North-West Pacific boundary layer exhibits a fast ascent to the upper troposphere within 2 days. This behavior is attributed to a warm conveyor belt using the criteria published by Eckhardt et al. (2004). Satellite images show that the ascending part of the trajectory is near the warm front of a cyclone that is located about 2000 km south of the peninsula of Kamchatka (North-West Pacific Ocean). Warm conveyor belts are known to be the most important extra-tropical transport mechanism of water vapor to the free and upper troposphere, although the water vapor flux moves like a jet from a rather restricted area (Browning and Roberts, 1994; Browning et al., 1997; Eckhardt et al., 2004; Ziv et al., 2009). It is remarkable that these filamentary structures are partially preserved, while traveling around half the hemisphere. A wind speed of 16 m s^{-1} at an altitude of 4.5 km (Munich radiosonde, 12:00 UTC) transforms a time shift of two hours into a horizontal

shift of about 115 km. The water vapor density at this altitude changes by more than a factor of 5 within 2 h in this case.

5.2.2 General discussion

It is reasonable to assume that much of the variability in the free troposphere is caused by the rich layer structure advected along or in the vicinity of the North Atlantic storm track or from the Mediterranean basin and North Africa. From our lidar measurements of ozone, water vapor, and aerosol, we know that the persistence of specific free tropospheric layers above our site can range from less than one hour to more than one day (Eisele et al., 1999; Stohl and Trickl, 1999; Trickl et al., 2003; Trickl et al., 2010, 2011). Along the jet stream, a lot of different ascending and descending air streams merge or separate (e.g. Appenzeller et al., 1996; Stohl, 2001; Cooper et al., 2001, 2002, 2004b, a; Flentje et al., 2005). The advection of filamentary and heterogeneous layer structures affects the entire free troposphere and dominates the variability of water vapor in the upper troposphere above 5 km. The most important source regions contributing to observations above our site have been the stratosphere (very dry air), North America, the (sub)tropical Atlantic (very humid), but also Asia. Sometimes, dry and ozone-rich air flows along the northward spiraling subtropical jet streams (Trickl et al., 2011). The layers frequently possess a meridional component, leading to a transverse passage of adjacent layers across the observational site. This implies a rapid change in concentrations.

6 Summary and conclusions

The result of our studies is a quantitative description of the short-term variability of water vapor in the free troposphere above Mt. Zugspitze, which is a location representative of Central Europe. From measurement data recorded with two high-precision optical water vapor sounders arranged in a unique pointing geometry, we derived in-

[Title Page](#)

[Abstract](#)

[Introduction](#)

[Conclusions](#)

[References](#)

[Tables](#)

[Figures](#)

◀

▶

◀

▶

[Back](#)

[Close](#)

[Full Screen / Esc](#)

[Printer-friendly Version](#)

[Interactive Discussion](#)



formation about the spatio-temporal variability of integrated water vapor (IWV) on the 1 km-scale and on the minutes scale.

Within a time interval of 20 min, a variability of about 0.35 mm was determined in the summer season under the condition of good volume matching ($\Delta x < 2\text{ km}$). The spatial variability became significant for horizontal distances above 2 km, but only in the warm season. The variability of IWV observed in the winter season generally was lower and did not increase with a horizontal mismatch of the probed volume ($\Delta x < 12\text{ km}$). Its relative value, however, was larger than in the summer season. The seasonality of the IWV short-term variability and the geometrical restrictions of the measurements underline that local convection is the main source of variability in the summer season, while the variability in the winter season is driven by dynamics on a larger scale. The temporal variability of IWV was determined to be 0.05 mm on the minute scale (5 min) with a uniform increase to 0.5 mm on the time scale of one day.

The free tropospheric profile variability of water vapor on the time scale of hours (e.g., 1–5 h) shows a broad minimum around 4.5 km a.s.l. and much larger values for higher altitudes with a constant increase up to the tropopause region. Longer time intervals generally yield larger variations at all altitudes and additionally show a more significant maximum at the lower edge of the measurement range (3 km). These findings are explained by the vertical wind profile and the heterogeneity of air masses within the upper air flow advected with a high velocity and, additionally, by the impact of local convection below 4.5 km. The covariance matrix of the profile variability yields information about the connectivity of neighboring layers and shows that the air flow below 6 km is rather incoherent, while the upper air stream above 8 km is much more coherent.

We presented 4 case studies in which the profile variability of water vapor on the time scale of hours was attributed to specific mechanisms: local and vertically limited convection under stable conditions, high-reaching convection under unstable conditions, downwelling of a stratospheric intrusion, and long-range transport from very different source regions.

Spatio-temporal variability of water vapor

H. Vogelmann et al.

[Title Page](#)

[Abstract](#)

[Introduction](#)

[Conclusions](#)

[References](#)

[Tables](#)

[Figures](#)

[|◀](#)

[▶|](#)

[◀](#)

[▶](#)

[Back](#)

[Close](#)

[Full Screen / Esc](#)

[Printer-friendly Version](#)

[Interactive Discussion](#)



Spatio-temporal variability of water vapor

H. Vogelmann et al.

[Title Page](#)

[Abstract](#)

[Introduction](#)

[Conclusions](#)

[References](#)

[Tables](#)

[Figures](#)

[◀](#)

[▶](#)

[◀](#)

[▶](#)

[Back](#)

[Close](#)

[Full Screen / Esc](#)

[Printer-friendly Version](#)

[Interactive Discussion](#)



The source of the variability can be either local convection or long-range transport of inhomogeneous air masses. When reviewing all profiles of our study, we found that it is not always possible to distinguish clearly between both mechanisms of short-term variability. In particular, for altitudes below 5 km, which are potentially affected by local convection even under stable atmospheric conditions, we have to assume a mixture of both local contributions and the advection of inhomogeneous layer structures from different remote source regions. From cases where a clear assignment was possible, we conclude that the long-range advection of very inhomogeneous layer structures can cause relatively short-term variations of the water vapor concentration at a certain altitude, which are larger by one order of magnitude than variations in cases dominated by the impact of local convection.

In spite of the missing convection, the relatively short-term variability of water vapor (IWV and profiles) is higher during the winter season. This is explained by the results of (Trickl et al., 2010), according to which most stratospheric intrusions pass Mt. Zugspitze between 2 and 4 km a.s.l., primarily during the winter season. Roughly 3/4 of them reach the Zugspitze summit (2962 m) and were detected directly by the in-situ instrumentation.

Our results for the first time provide for a quantitative description of the free tropospheric spatio-temporal variability of water vapor on the scales of minutes and kilometers (horizontal) for IWV and the scales of hours and 500 m (vertical) for profiles. This information can be useful for the parameterization of humidity in atmospheric models as well as for estimating the influence of the atmospheric variability of water vapor on the significance of water vapor measurements performed with a given integration time. In a related sense our results also provide the information necessary for evaluating intercomparison studies of not perfectly co-located or synchronized instruments. Our findings fit perfectly to the results of our previous intercomparison study (Vogelmann et al., 2011) that already indicated a high variability of water vapor, as a result of which very tight matching criteria are required down to the scales of 10 min and several hundred meters to reduce co-location-effects to a negligible level.

Spatio-temporal variability of water vapor

H. Vogelmann et al.

[Title Page](#)

[Abstract](#)

[Introduction](#)

[Conclusions](#)

[References](#)

[Tables](#)

[Figures](#)

◀

▶

◀

▶

[Back](#)

[Close](#)

[Full Screen / Esc](#)

[Printer-friendly Version](#)

[Interactive Discussion](#)



Acknowledgements. We thank Hans-Peter Schmid (KIT/IMK-IFU) for his continuous interest in this work and M. Rettinger (KIT/IMK-IFU) for executing the FITR measurements at Mt. Zugspitze. We also acknowledge the team of the Schneefernerhaus research station (UFS) for maintaining our lidar measurements and the Bavarian Ministry of Environment and Consumer Protection for funding our work within the ALOMAR cooperation.

The service charges for this open access publication have been covered by a Research Centre of the Helmholtz Association.

10 References

- Adam, M., Demoz, B. B., Whiteman, D. N., Venable, D. D., Joseph, E., Gambacorta, A., Wei, J., Shephard, M. W., Miloshevich, L. M., Barnet, C. D., Herman, R. L., Fitzgibbon, J., and Connell, R.: Water vapor measurements by Howard University Raman Lidar during the WAVES 2006 Campaign, *J. Atmos. Ocean. Tech.*, 27, 42–60, doi:10.1175/2009JTECHA1331.1, 2010. 28235
- Appenzeller, C., Davies, H. C., and Norton, W. A.: Fragmentation of stratospheric intrusions, *J. Geophys. Res.*, 101, 1435–1456, doi:10.1029/95JD02674, 1996. 28248
- Birner, T., Dörnbrack, A., and Schumann, U.: How sharp is the tropopause at midlatitudes?, *Geophys. Rev. Lett.*, 29, 1700, doi:10.1029/2002GL015142, 2002. 28242
- Bleisch, R., Kämpfer, N., and Haefele, A.: Retrieval of tropospheric water vapour by using spectra of a 22 GHz radiometer, *Atmos. Meas. Tech.*, 4, 1891–1903, doi:10.5194/amt-4-1891-2011, 2011. 28235
- Browning, K. A. and Roberts, N. M.: Structure of a frontal cyclone, *Q. J. Roy. Meteor. Soc.*, 120, 1535–1557, doi:10.1002/qj.49712052006, 1994. 28247
- Browning, K. A., Roberts, N. M., and Illingworth, A. J.: Mesoscale analysis of the activation of a cold front during cyclogenesis, *Q. J. Roy. Meteor. Soc.*, 123, 2349–2375, doi:10.1002/qj.49712354410, 1997. 28247
- Carnuth, W. and Trickl, T.: Transport studies with the IFU three-wavelength aerosol lidar during the VOTALP Mesolcina experiment, *Atmos. Environ.*, 34, 1425–1434, 2000. 28240, 28245

- Carnuth, W., Kempfer, U., and Trickl, T.: Highlights of the tropospheric lidar studies at IFU within the TOR project, Tellus B, 54, 163–185, 2002. 28240, 28245
- Cooper, O. R., Moody, J. L., Parrish, D. D., Trainer, M., Ryerson, T. B., Holloway, J. S., Hübler, G., Fehsenfeld, F. C., Oltmans, S. J., and Evans, M. J.: Trace gas signatures of the airstreams within North Atlantic cyclones: case studies from the North Atlantic Regional Experiment (NARE 97) aircraft intensive, J. Geophys. Res., 106, 5437–5456, doi:10.1029/2000JD900574, 2001. 28248
- Cooper, O. R., Moody, J. L., Parrish, D. D., Trainer, M., Holloway, J. S., Hübler, G., Fehsenfeld, F. C., and Stohl, A.: Trace gas composition of midlatitude cyclones over the western North Atlantic Ocean: a seasonal comparison of O₃ and CO, J. Geophys. Res., 107, 4057, doi:10.1029/2001JD000902, 2002. 28248
- Cooper, O., Forster, C., Parrish, D., Dunlea, E., Hübler, G., Fehsenfeld, F., Holloway, J., Oltmans, S., Johnson, B., Wimmers, A., and Horowitz, L.: On the life cycle of a stratospheric intrusion and its dispersion into polluted warm conveyor belts, J. Geophys. Res., 109, D23S09, doi:10.1029/2003JD004006, 2004a. 28248
- Cooper, O. R., Forster, C., Parrish, D., Trainer, M., Dunlea, E., Ryerson, T., Hübler, G., Fehsenfeld, F., Nicks, D., Holloway, J., de Gouw, J., Warneke, C., Roberts, J. M., Flocke, F., and Moody, J.: A case study of transpacific warm conveyor belt transport: influence of merging airstreams on trace gas import to North America, J. Geophys. Res., 109, D23S08, doi:10.1029/2003JD003624, 2004b. 28248
- Draxler, R. R. and Hess, G. D.: An overview of the HYSPLIT_4 modelling system for trajectories, dispersion, and deposition, Aust. Meteorol. Mag., 47, 295–308, 1998. 28244
- Eckhardt, S., Stohl, A., Wernli, H., James, P., Forster, C., and Spichtinger, N.: A 15-year climatology of warm conveyor belts., J. Climate, 17, 218–237, doi:10.1175/1520-0442(2004)017<0218:AYCOWC>2.0.CO;2, 2004. 28247
- Eisele, H., Scheel, H. E., Sládkovič, R., and Trickl, T.: High-resolution lidar measurements of stratosphere–troposphere exchange, J. Atmos. Sci., 56, 319–330, 1999. 28234, 28248
- Fassò, A., Ignaccolo, R., Madonna, F., Demoz, B. B., and Franco-Villoria, M.: Statistical modelling of collocation uncertainty in atmospheric thermodynamic profiles, Atmos. Meas. Tech., 7, 1803–1816, doi:10.5194/amt-7-1803-2014, 2014. 28235
- Flentje, H., Dörnbrack, A., Ehret, G., Fix, A., Kiemle, C., Poberaj, G., and Wirth, M.: Water vapor heterogeneity related to tropopause folds over the North Atlantic revealed

Spatio-temporal variability of water vapor

H. Vogelmann et al.

[Title Page](#)[Abstract](#)[Introduction](#)[Conclusions](#)[References](#)[Tables](#)[Figures](#)[|◀](#)[▶|](#)[◀](#)[▶](#)[Back](#)[Close](#)[Full Screen / Esc](#)[Printer-friendly Version](#)[Interactive Discussion](#)

- by airborne water vapor differential absorption lidar, *J. Geophys. Res.*, 110, D03115, doi:10.1029/2004JD004957, 2005. 28248
- Harries, J. E.: Atmospheric radiation and atmospheric humidity, *Q. J. Roy. Meteor. Soc.*, 123, 2173–2186, 1997. 28233
- Immler, F. J., Dykema, J., Gardiner, T., Whiteman, D. N., Thorne, P. W., and Vömel, H.: Reference Quality Upper-Air Measurements: guidance for developing GRUAN data products, *Atmos. Meas. Tech.*, 3, 1217–1231, doi:10.5194/amt-3-1217-2010, 2010. 28235
- Kiehl, J. T. and Trenberth, K. E.: Earth's annual global mean energy budget, *B. Am. Meteorol. Soc.*, 78, 197–208, 1997. 28233
- Kreipl, S.: Messung des Aerosoltransports am Alpennordrand mittels Laserradar (Lidar), Ph.D. thesis, Universität Erlangen, 2006 (in German). 28240, 28245
- Kämpfer, N. (Ed.): Monitoring Atmospheric Water Vapour – Ground-Based Remote Sensing and In-situ Methods, Springer, Berlin, Heidelberg, 2013. 28234
- Leblanc, T., Walsh, T. D., McDermid, I. S., Toon, G. C., Blavier, J.-F., Haines, B., Read, W. G., Herman, B., Fetzer, E., Sander, S., Pongetti, T., Whiteman, D. N., McGee, T. G., Twigg, L., Sumnicht, G., Venable, D., Calhoun, M., Dirisu, A., Hurst, D., Jordan, A., Hall, E., Miloshevich, L., Vömel, H., Straub, C., Kampfer, N., Nedoluha, G. E., Gomez, R. M., Holub, K., Gutman, S., Braun, J., Vanhove, T., Stiller, G., and Hauchecorne, A.: Measurements of Humidity in the Atmosphere and Validation Experiments (MOHAVE)-2009: overview of campaign operations and results, *Atmos. Meas. Tech.*, 4, 2579–2605, doi:10.5194/amt-4-2579-2011, 2011. 28235
- Müller, H., and Reiter, R.: Untersuchung der Gebirgsgrenzschicht über einem großen Alpental bei Berg-Talwindzirkulation, *Meteorol. Rundsch.*, 39, 247–256, 1986 (in German). 28240
- Pougatchev, N. S., Connor, B. J., and Rinsland, C. P.: Infrared measurements of the ozone vertical distribution above Kitt Peak, *J. Geophys. Res.*, 100, 16689–16697, doi:10.1029/95JD01296, 1995. 28236
- Reiter, R., Müller, H., Sladkovic, R., and Munzert, K.: Aerologische Untersuchungen der tages-periodischen Gebirgswinde unter besonderer Berücksichtigung des Windfeldes im Talquerschnitt, *Meteorol. Rundsch.*, 36, 225–242, 1983 (in German). 28240
- Riehl, H.: Jet Streams of the Atmosphere, Tech. Rep. 32, Department of Atmospheric Science, Colorado State University, Fort Collins, Colorado, 1962. 28242
- Seidel, D. J., Sun, B., Pettey, M., and Reale, A.: Global radiosonde balloon drift statistics, *J. Geophys. Res.*, 116, D07102, doi:10.1029/2010JD014891, 2011. 28235

Spatio-temporal variability of water vapor

H. Vogelmann et al.

[Title Page](#)

[Abstract](#)

[Introduction](#)

[Conclusions](#)

[References](#)

[Tables](#)

[Figures](#)

◀

▶

◀

▶

[Back](#)

[Close](#)

[Full Screen / Esc](#)

[Printer-friendly Version](#)

[Interactive Discussion](#)



Soden, B. J. and Lanzante, J. R.: An assessment of satellite and radiosonde climatologies of upper-tropospheric water vapor, *J. Climate*, 9, 1235–1250, doi:10.1175/1520-0442(1996)009<1235:AAOSAR>2.0.CO;2, 1996. 28235

Stiller, G. P., Kiefer, M., Eckert, E., von Clarmann, T., Kellmann, S., García-Comas, M.,
5 Funke, B., Leblanc, T., Fetzer, E., Froidevaux, L., Gomez, M., Hall, E., Hurst, D., Jordan, A., Kämpfer, N., Lambert, A., McDermid, I. S., McGee, T., Miloshevich, L., Nedoluha, G., Read, W., Schneider, M., Schwartz, M., Straub, C., Toon, G., Twigg, L. W., Walker, K., and Whiteman, D. N.: Validation of MIPAS IMK/IAA temperature, water vapor, and ozone profiles with MOHAVE-2009 campaign measurements, *Atmos. Meas. Tech.*, 5, 289–320, doi:10.5194/amt-5-289-2012, 2012. 28235

Stohl, A.: A 1-year Lagrangian “climatology” of airstreams in the Northern Hemisphere troposphere and lowermost stratosphere, *J. Geophys. Res.*, 106, 7263–7280, doi:10.1029/2000JD900570, 2001. 28248

Stohl, A. and Trickl, T.: A textbook example of long-range transport: simultaneous observation of ozone maxima of stratospheric and North American origin in the free troposphere over Europe, *J. Geophys. Res.*, 104, 30445–30462, doi:10.1029/1999JD900803, 1999. 28234,
15 28248

Stohl, A., Spichtinger-Rakowsky, N., Bonasoni, P., Feldmann, H., Memmesheimer, M., Scheel, H. E., Trickl, T., Hübener, S., Ringer, W., and Mandl, M.: The influence of stratospheric intrusions on alpine ozone concentrations, *Atmos. Environ.*, 34, 1323–1354, doi:10.1016/S1352-2310(99)00320-9, 2000. 28247

Sun, B., Reale, A., Seidel, D. J., and Hunt, D. C.: Comparing radiosonde and COSMIC atmospheric profile data to quantify differences among radiosonde types and the effects of imperfect collocation on comparison statistics, *J. Geophys. Res.*, 115, D23104, doi:10.1029/2010JD014457, 2010. 28235

Sussmann, R. and Schäfer, K.: Infrared spectroscopy of tropospheric trace gases: combined analysis of horizontal and vertical column abundances, *Appl. Optics*, 36, 735–741, doi:10.1364/AO.36.000735, 1997. 28236

Sussmann, R., Borsdorff, T., Rettinger, M., Camy-Peyret, C., Demoulin, P., Duchatelet, P.,
30 Mahieu, E., and Servais, C.: Technical Note: Harmonized retrieval of column-integrated atmospheric water vapor from the FTIR network – first examples for long-term records and station trends, *Atmos. Chem. Phys.*, 9, 8987–8999, doi:10.5194/acp-9-8987-2009, 2009. 28234, 28235, 28236

Title Page	
Abstract	Introduction
Conclusions	References
Tables	Figures
◀	▶
◀	▶
Back	Close
Full Screen / Esc	
Printer-friendly Version	
Interactive Discussion	



Tobin, D. C., Revercomb, H. E., Knuteson, R. O., Lesht, B. M., Strow, L. L., Hannon, S. E., Feltz, W. F., Moy, L. A., Fetzer, E. J., and Cress, T. S.: Atmospheric Radiation Measurement site atmospheric state best estimates for Atmospheric Infrared Sounder temperature and water vapor retrieval validation, *J. Geophys. Res.*, 111, D09S14, doi:10.1029/2005JD006103, 2006. 28235

Trenberth, K. E.: Atmospheric moisture residence times and cycling: implications for rainfall rates and climate change, *Clim. Change*, 39, 667–694, doi:10.1023/A:1005319109110, 1998. 28233

Trenberth, K., Jones, P., Ambenje, P., Bojariu, R., Easterling, D., Tank, A., Parker, D., Rahimzadeh, F., Renwick, J., Rusticucci, M., Soden, B., and Zhai, P.: Observations: surface and atmospheric climate change, in: *Climate Change 2007: The Physical Science Basis. Contribution of Working Group I to the Fourth Assessment Report of the Intergovernmental Panel on Climate Change*, Cambridge University Press, Cambridge, UK and New York, NY, USA, chap. 3, 235–336, 2007. 28233

Trickl, T., Cooper, O. R., Eisele, H., James, P., Mücke, R., and Stohl, A.: Intercontinental transport and its influence on the ozone concentrations over central Europe: three case studies, *J. Geophys. Res.*, 108, 8530, doi:10.1029/2002JD002735, 2003. 28234, 28248

Trickl, T., Feldmann, H., Kanter, H.-J., Scheel, H.-E., Sprenger, M., Stohl, A., and Wernli, H.: Forecasted deep stratospheric intrusions over Central Europe: case studies and climatologies, *Atmos. Chem. Phys.*, 10, 499–524, doi:10.5194/acp-10-499-2010, 2010. 28234, 28247, 28248, 28250

Trickl, T., Bärtsch-Ritter, N., Eisele, H., Furger, M., Mücke, R., Sprenger, M., and Stohl, A.: High-ozone layers in the middle and upper troposphere above Central Europe: potential import from the stratosphere along the subtropical jet stream, *Atmos. Chem. Phys.*, 11, 9343–9366, doi:10.5194/acp-11-9343-2011, 2011. 28234, 28248

Trickl, T., Vogelmann, H., Giehl, H., Scheel, H.-E., Sprenger, M., and Stohl, A.: How stratospheric are deep stratospheric intrusions?, *Atmos. Chem. Phys.*, 14, 9941–9961, doi:10.5194/acp-14-9941-2014, 2014. 28247

Turner, D. D. and Mlawer, E. J.: The radiative heating in underexplored bands campaigns, *B. Am. Meteorol. Soc.*, 91, 911–923, doi:10.1175/2010BAMS2904.1, 2010. 28233

Vogelmann, H. and Trickl, T.: Wide range sounding of free tropospheric water vapor with a Differential Absorption Lidar (DIAL) at a high altitude station, *Appl. Optics*, 47, 2116–2132, doi:10.1364/AO.47.002116, 2008. 28234, 28237

Spatio-temporal variability of water vapor

H. Vogelmann et al.

[Title Page](#)

[Abstract](#)

[Introduction](#)

[Conclusions](#)

[References](#)

[Tables](#)

[Figures](#)

◀

▶

◀

▶

[Back](#)

[Close](#)

[Full Screen / Esc](#)

[Printer-friendly Version](#)

[Interactive Discussion](#)



- Vogelmann, H., Sussmann, R., Trickl, T., and Borsdorff, T.: Intercomparison of atmospheric water vapor soundings from the differential absorption lidar (DIAL) and the solar FTIR system on Mt. Zugspitze, *Atmos. Meas. Tech.*, 4, 835–841, doi:10.5194/amt-4-835-2011, 2011. 28234, 28235, 28237, 28239, 28241, 28250
- 5 Wagner, T., Beirle, S., Grzegorski, M., and Platt, U.: Global trends (1996–2003) of total column precipitable water observed by Global Ozone Monitoring Experiment (GOME) on ERS-2 and their relation to near-surface temperature, *J. Geophys. Res.*, 111, D12102, doi:10.1029/2005JD006523, 2006. 28233
- 10 Whiteman, D. N., Russo, F., Demoz, B., Miloshevich, L. M., Veselovskii, I., Hannon, S., Wang, Z., Vömel, H., Schmidlin, F., Lesht, B., Moore, P. J., Beebe, A. S., Gambacorta, A., and Barnet, C.: Analysis of Raman lidar and radiosonde measurements from the AWEX-G field campaign and its relation to Aqua validation, *J. Geophys. Res.*, 111, D09S09, doi:10.1029/2005JD006429, 2006. 28235
- 15 Wirth, M., Fix, A., Ehret, G., Reichardt, J., Begie, R., Engelbart, D., Vömel, H., Calpini, B., Romanens, G., Apituley, A., Wilson, K. M., Vogelmann, H., and Trickl, T.: Intercomparison of airborne water vapour DIAL measurements with ground based remote sensing and radiosondes within the Framework of LUAMI 2008, in: Proceedings of the 8th International Symposium on Tropospheric Profiling, edited by: Apituley, A., Russchenberg, H., and Monna, W., Delft, the Netherlands, poster presentation, 2009. 28235
- 20 Ziv, B., Saaroni, H., Romem, M., Heifetz, E., Harnik, N., and Baharad, A.: Analysis of conveyor belts in winter Mediterranean cyclones, *Theor. Appl. Climatol.*, 99, 441–455, doi:10.1007/s00704-009-0150-9, 2009. 28247

Spatio-temporal variability of water vapor

H. Vogelmann et al.

[Title Page](#)

[Abstract](#)

[Introduction](#)

[Conclusions](#)

[References](#)

[Tables](#)

[Figures](#)

◀

▶

◀

▶

[Back](#)

[Close](#)

[Full Screen / Esc](#)

[Printer-friendly Version](#)

[Interactive Discussion](#)



Table 1. Specifications of the FTIR and the DIAL on Mt. Zugspitze.

	FTIR	DIAL
Geographical Coordinates	10°59'8.7" E 47°25'15.6" N	10°58'46.8" E 47°25'0" N
Altitude a.s.l.	2964 m	2675 m
Vertical range a.s.l.	above 2.96 km	2.95–12 km
Typ. integration time	13.3 min	17 min
Spectral range [cm ⁻¹]	micro windows 839.5–840.5 849.0–850.2 852.0–853.1	v_{on} 12 236.560 12 237.466 12 243.537

[Title Page](#)[Abstract](#)[Introduction](#)[Conclusions](#)[References](#)[Tables](#)[Figures](#)[|◀](#)[▶|](#)[◀](#)[▶](#)[Back](#)[Close](#)[Full Screen / Esc](#)[Printer-friendly Version](#)[Interactive Discussion](#)

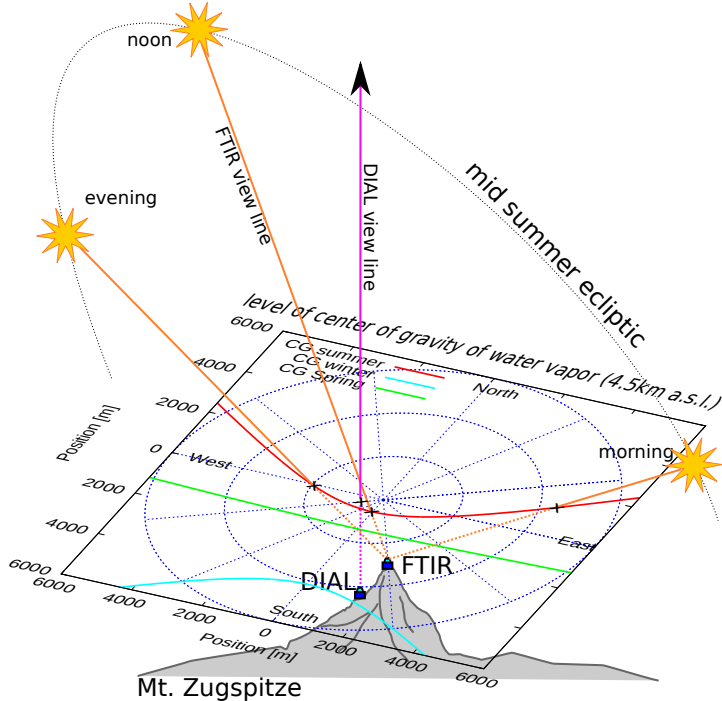


Figure 1. Geometrical setup of the IWV intercomparison between DIAL and FTIR on Mt. Zugspitze. The DIAL is located 680 m to the south-west of the FTIR and 288 m below. The horizontal coordinate grid plane (CG-plane) marks the mean altitude of the center of gravity of the water vapor distribution above Mt. Zugspitze (see text) and has its point of origin vertical above the FTIR. The red, green, and blue curves in the CG-plane are the trajectories of the points, where the view line (e.g., orange lines from FTIR to the sun in the case of midsummer) of the FTIR meets the CG-plane in midsummer, spring, and midwinter. Consequently, the trajectories mark the horizontal position of the center of gravity of the vertical water vapor distribution measured by the FTIR. The pink line marks the static and vertical view line of the DIAL.

28258

**Spatio-temporal
variability of water
vapor**

H. Vogelmann et al.

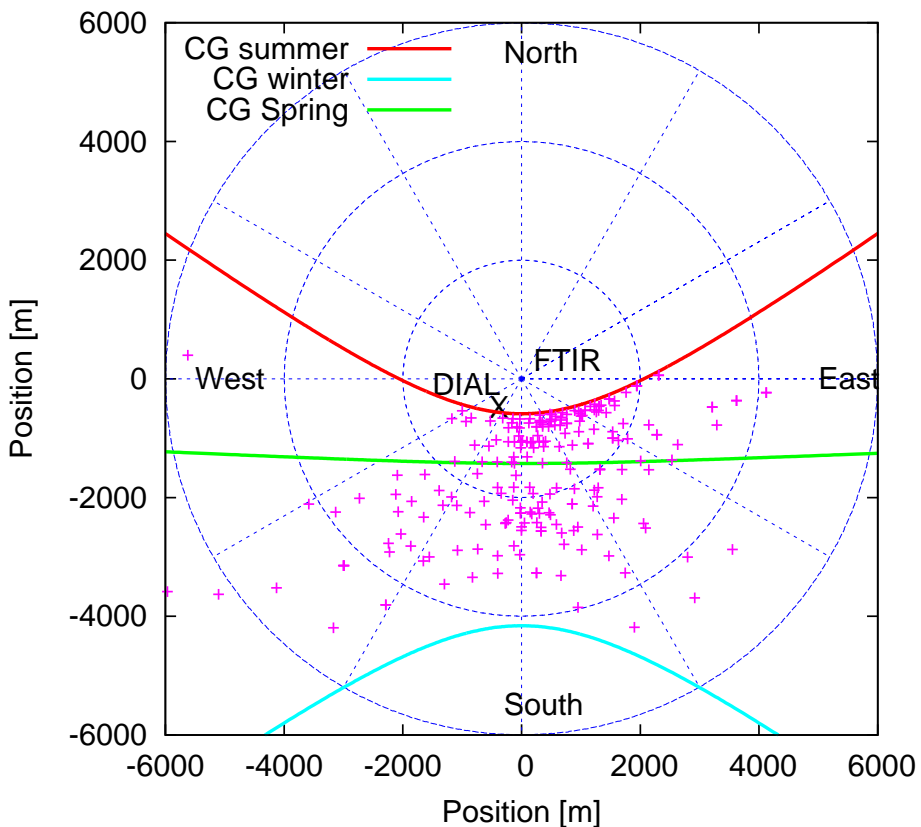


Figure 2. Trajectories of the horizontal positions of the center of gravity (CG) of the vertical water vapor distribution measured by the FTIR for IWV midsummer, spring, and midwinter. Center of gravity horizontal locations from FTIR measurements chronological coinciding with DIAL measurements ($\Delta t \leq 30\text{ min}$) are marked by crosses.

Title Page	
Abstract	Introduction
Conclusions	References
Tables	Figures
◀	▶
◀	▶
Back	Close
Full Screen / Esc	
Printer-friendly Version	
Interactive Discussion	



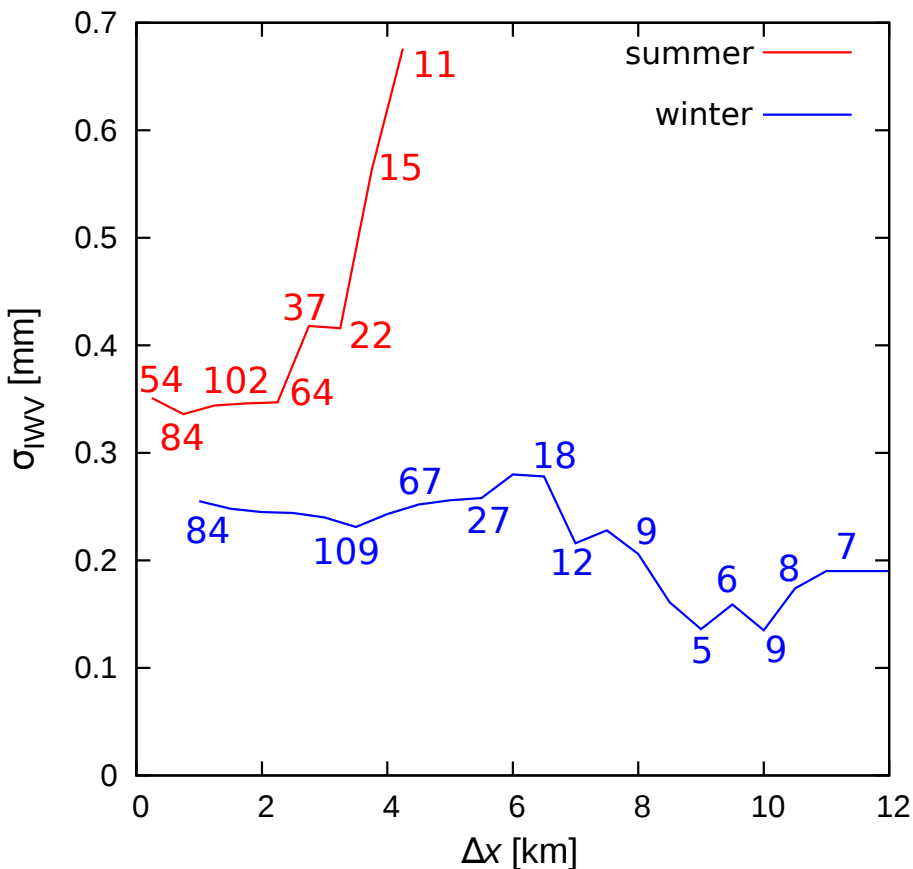


Figure 3. σ_{IWV} as a function of the horizontal distance Δx between the center of gravity of FTIR IWV and DIAL IWV in the summer season (red) and in the winter season (blue). The coincidence time interval is 60 min for both curves ($\Delta t = 60$ min). For geometrical reasons, the shortest distance in the winter season is 1 km. The quantity of measurement pairs from which σ_{IWV} was calculated is indicated by the numbers near the curves (not for all nodes).

**Spatio-temporal
variability of water
vapor**

H. Vogelmann et al.

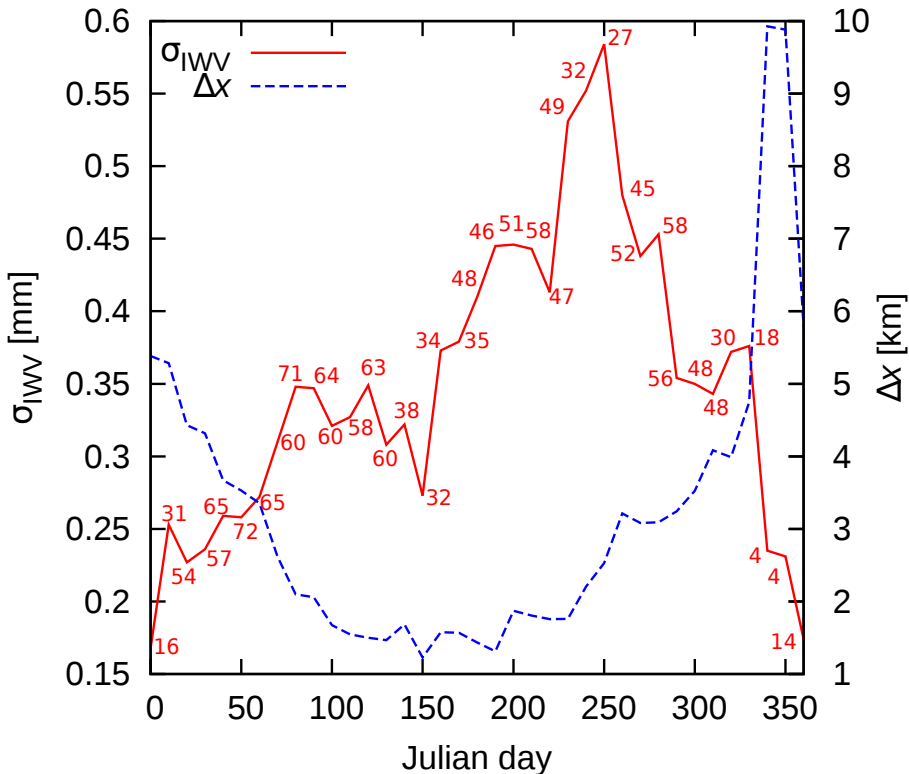


Figure 4. σ_{IWV} as a function of Julian day. The coincidence interval is 20 min in this case, pairs within 30 days were taken into account. The quantity of measurement pairs from which σ_{IWV} was calculated is indicated by the numbers near the curve. The dashed line shows the mean horizontal distance between the pairwise soundings of IWV as a function of the season.

- [Title Page](#)
- [Abstract](#) | [Introduction](#)
- [Conclusions](#) | [References](#)
- [Tables](#) | [Figures](#)
- [◀](#) | [▶](#)
- [◀](#) | [▶](#)
- [Back](#) | [Close](#)
- [Full Screen / Esc](#)
- [Printer-friendly Version](#)
- [Interactive Discussion](#)



Spatio-temporal variability of water vapor

H. Vogelmann et al.

The figure shows the correlation length σ_{WW} [mm] on the y-axis (ranging from 0 to 0.7) versus the coincidence interval [min] on a logarithmic x-axis (ranging from 1 to 1000). Three data series are plotted: 'all' (red line), 'azimuth = $210^0 \pm 6^0$ ' (green line), and 'FTIR-autocorrelation' (blue line). Data points are labeled with their values:

Coincidence interval [min]	σ_{WW} [mm] (all)	σ_{WW} [mm] (azimuth)	σ_{WW} [mm] (FTIR)
3	0.43	0.03	-
5	0.40	0.05	-
9	0.39	0.09	-
10	0.38	0.10	-
104	0.38	-	-
23	0.39	-	0.23
4086	0.40	0.24	0.24
56	0.43	-	0.27
839	0.44	0.28	0.28
10	0.45	0.30	0.28
110	0.46	-	0.35
1449	0.48	-	0.40
162	0.49	-	0.45
20799	0.50	-	0.48
2489	0.53	-	0.52
3205	0.65	-	0.58
35531	0.66	-	0.60

Figure 5. Variability as a function of the length of the time interval. The red curve shows σ_{IWV} from all measurements with no geometrical restrictions as a function of the length of the time interval in which data were taken into account. The green curve only includes measurements recorded in the early afternoon when the volume matching peaks with a sun azimuth of $210 \pm 6^\circ$. The blue curve only shows σ_{IWV} of IWV values from the FTIR instrument. The quantity of measurement pairs from which σ_{IWV} was calculated is indicated by the numbers near the curves (not for all nodes).

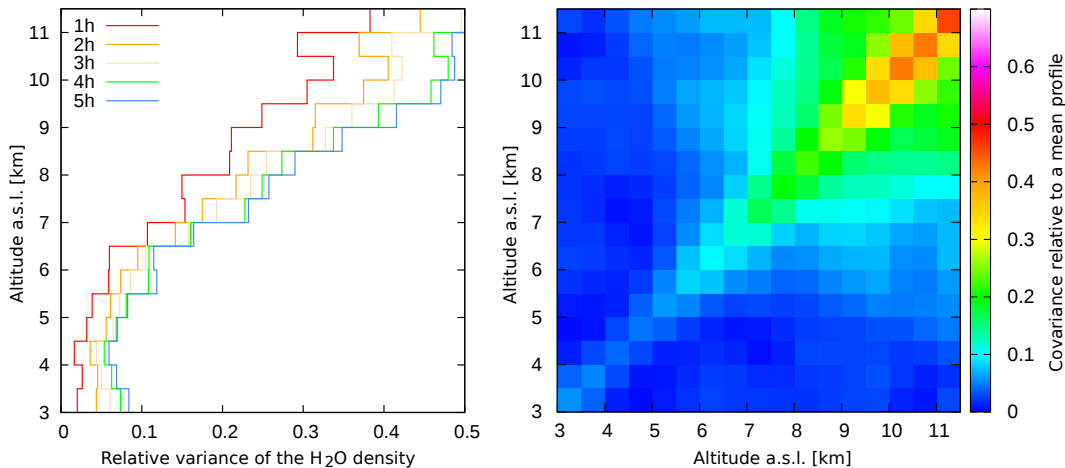


Figure 6. The short-term variability of the vertical water vapor profile is illustrated by the plot of the relative variance as a function of altitude within different time intervals (left plot). The covariance matrix (right plot) gives an idea of the interconnectivity of the variation between different altitudes.

Spatio-temporal variability of water vapor

H. Vogelmann et al.

- [Title Page](#)
- [Abstract](#) [Introduction](#)
- [Conclusions](#) [References](#)
- [Tables](#) [Figures](#)
- [◀](#) [▶](#)
- [◀](#) [▶](#)
- [Back](#) [Close](#)
- [Full Screen / Esc](#)
- [Printer-friendly Version](#)
- [Interactive Discussion](#)



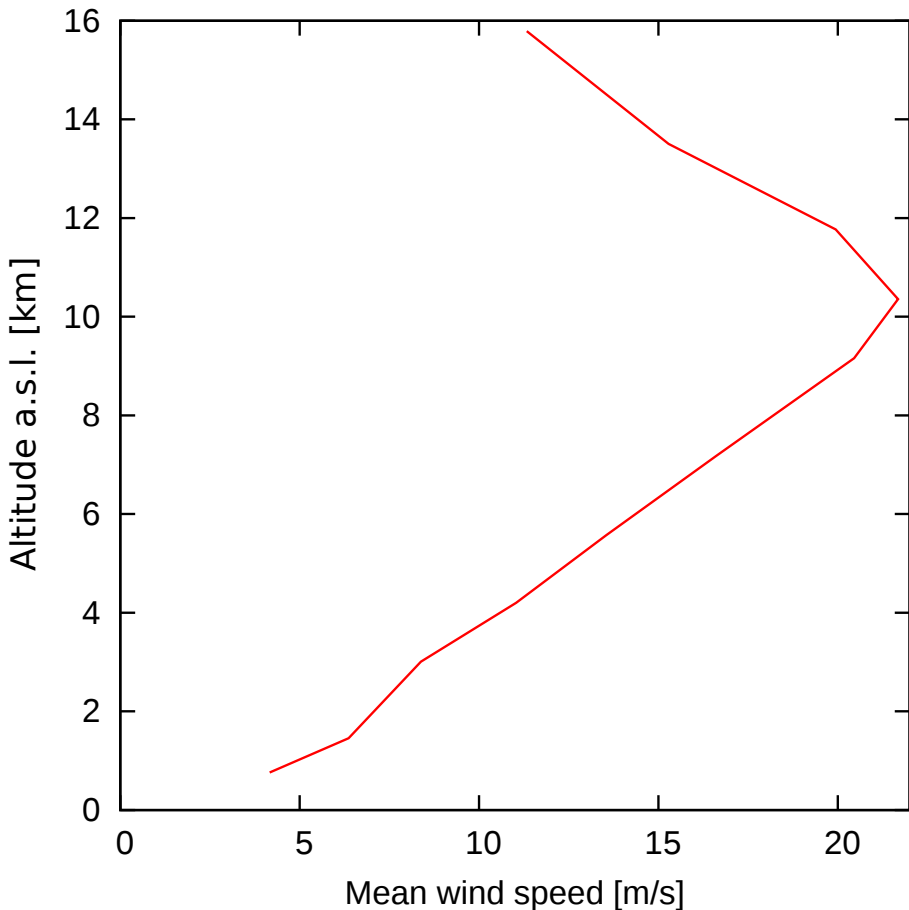


Figure 7. Mean wind speed above Mt. Zugspitze as a function of altitude (data from the National Center for Environmental Prediction, NCEP). Under the regime of the jet stream, the wind velocity at 10 km can occasionally exceed 100 m s^{-1} .

**Spatio-temporal
variability of water
vapor**

H. Vogelmann et al.

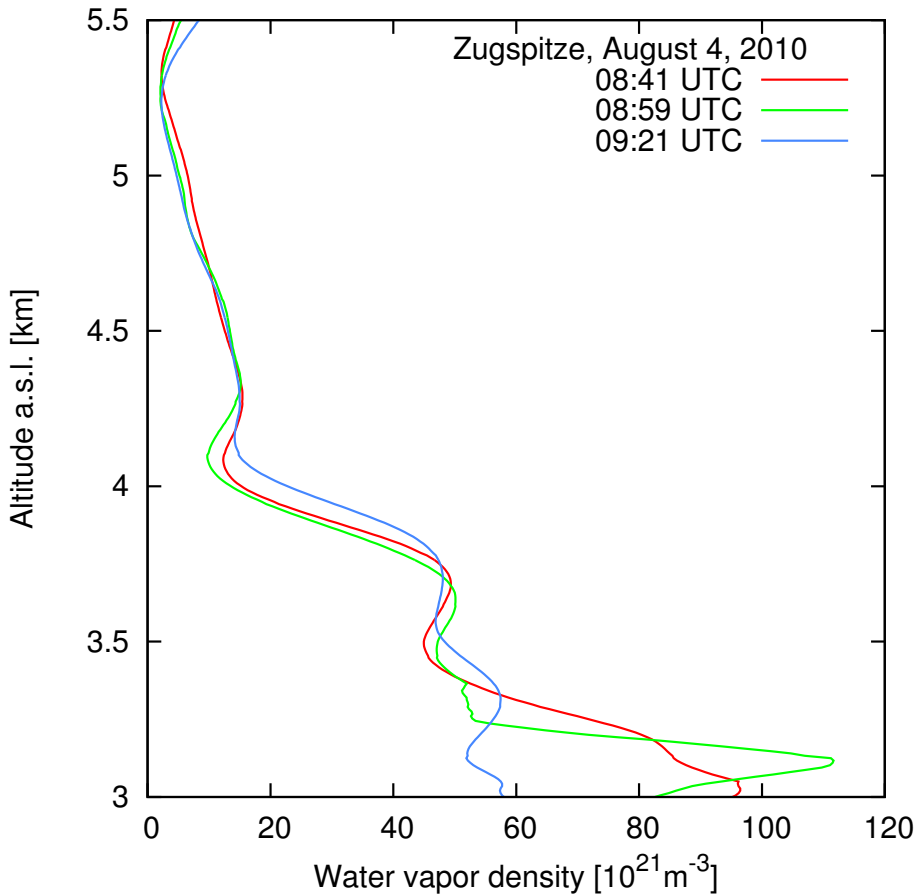


Figure 8. Short-term variability of the water vapor profile induced by local convection within a clearly confined upper edge of the boundary layer at 3.5 km under stable atmospheric conditions. The variations do not exceed a factor of 2.

**Spatio-temporal
variability of water
vapor**

H. Vogelmann et al.

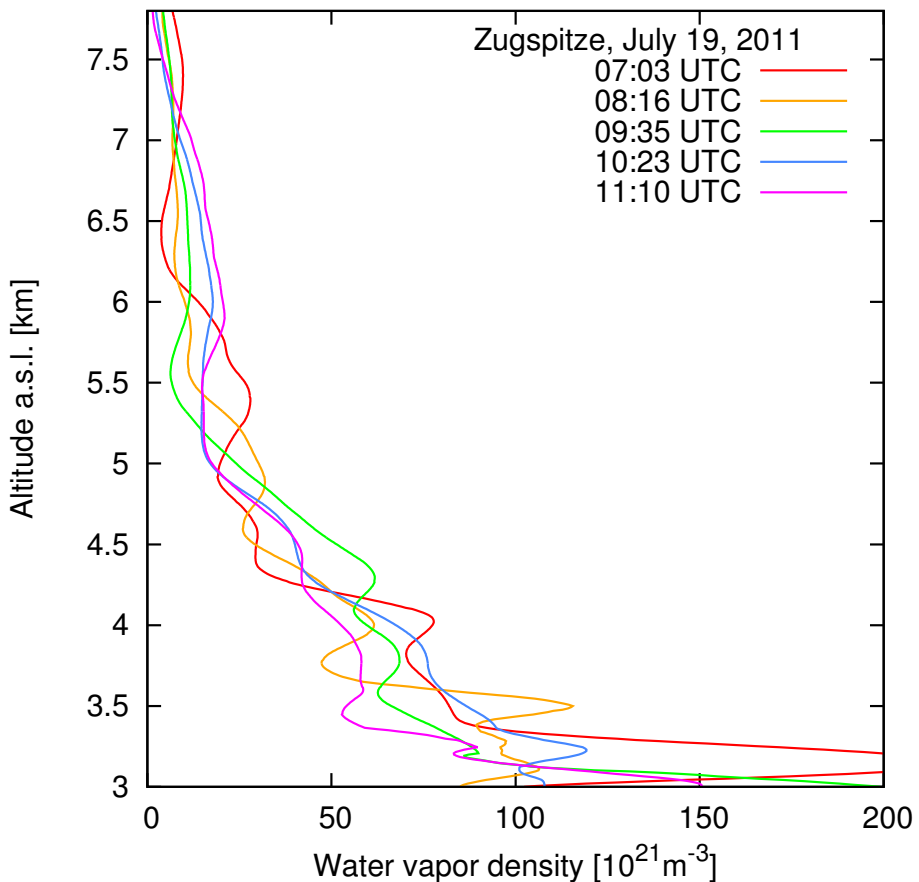


Figure 9. Short-term variability of the water vapor profile under atmospheric instability, high-reaching convection, and only a few hours before the formation of a thunderstorm.

**Spatio-temporal
variability of water
vapor**

H. Vogelmann et al.

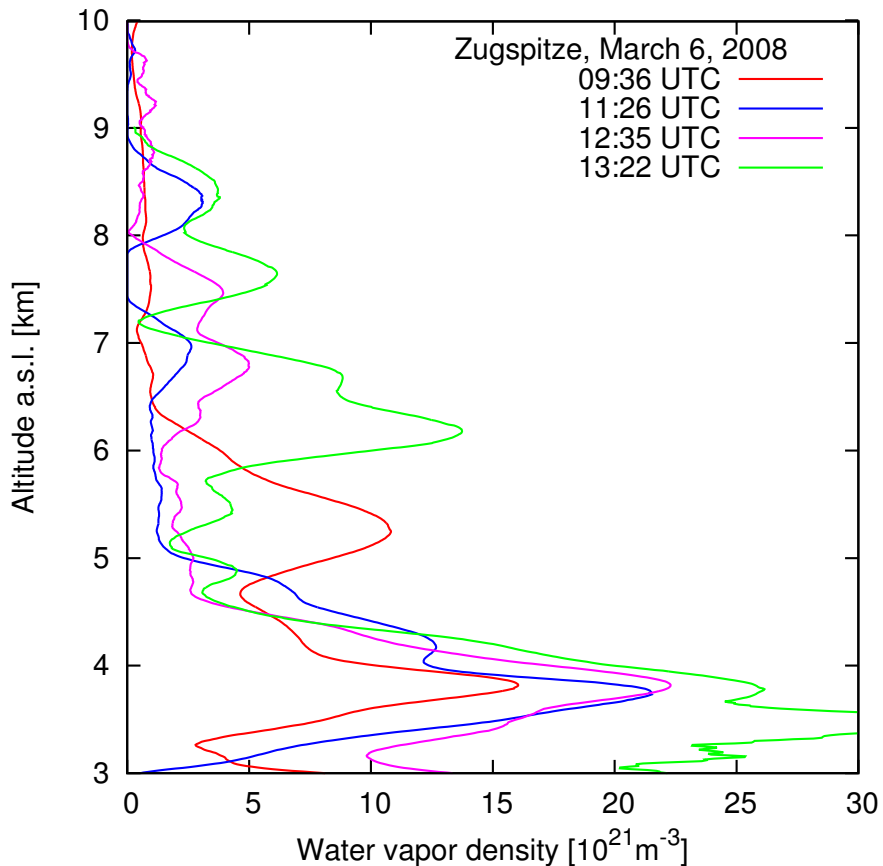


Figure 10. Example of extreme temporal variability of the vertical distribution of water vapor during a stratospheric intrusion event. Due to the advection velocity of about 11 m s^{-1} between 3 and 4 km altitude (data from radiosonde at Munich at 12:00 UTC, 100 km to the north) a time shift of 1 h corresponds to a horizontal shift of about 40 km within this altitude range.

Figure 11. Example of extreme variability of the vertical distribution of water vapor under rather humid conditions. Due to a wind speed of about 16 m s^{-1} at an altitude of 4.5 km (data from radiosonde Munich at 12:00 UTC, 100 km to the north) a time shift of 2 h corresponds to a horizontal shift of about 115 km at this altitude. The two profiles were recorded within less than two hours.